The Astrophysical Journal Letters, 924:L15 (7pp), 2022 January 1 https://doi.org/10.3847/2041-8213/ac460c

The Three-dimensional Collapse of a Rapidly Rotating 16 $M_\odot$ Star

C. E. Fields[1,2,3,4]
[1] Center for Theoretical Astrophysics, Los Alamos National Laboratory, Los Alamos, NM 87545, USA; carlnotsagan@lanl.gov
[2] Computer, Computational, and Statistical Sciences Division, Los Alamos National Laboratory, Los Alamos, NM 87545, USA
[3] X Computational Physics Division, Los Alamos National Laboratory, Los Alamos, NM 87545, USA
Received 2021 November 24; revised 2021 December 18; accepted 2021 December 23; published 2022 January 7

Abstract

I report on the three-dimensional (3D) hydrodynamic evolution of a rapidly rotating 16 $M_\odot$ star to iron core collapse. For the first time, I follow the 3D evolution of the angular momentum (AM) distribution in the iron core and convective shell burning regions for the final 10 minutes up to and including gravitational instability and core collapse. In 3D, convective regions show efficient AM transport that leads to an AM profile that differs in shape and magnitude from MESA within a few shell convective turnover timescales. For different progenitor models, such as those with tightly coupled Si/O convective shells, efficient AM transport in 3D simulations could lead to a significantly different AM distribution in the stellar interior affecting estimates of the natal neutron star or black hole spin. The results suggest that 3D AM transport in convective and rotating shell burning regions are critical components in models of massive stars and could *qualitatively* alter the explosion outcome and inferred compact remnant properties.

Unified Astronomy Thesaurus concepts: Stellar convective zones (301); Hydrodynamics (1963); Late stellar evolution (911); Massive stars (732); Supernovae (1668); Stellar rotation (1629)

1. Introduction

Massive stars are expected to rotate rapidly at their surface during the main sequence (MS; Fukuda 1982; de Mink et al. 2013; Ramírez-Agudelo et al. 2013). An important aspect of the subsequent evolutionary fate is the redistribution of angular momentum (AM) over its stellar lifetime. Heger et al. (2005) investigated the evolution of AM in 1D stellar evolution models with differential rotation and magnetic fields via the Spruit–Tayler (ST) dynamo (Spruit 2002). They found that magnetic torques provided an efficient mechanism for transport of AM out of the stellar core to provide remnant spin estimates that were largely in agreement with observations. Unfortunately, these models were limited by the treatment of convection and different mixing mechanisms which can only be approximated in 1D (Jones et al. 2017; Davis et al. 2019).

Convection has been studied somewhat extensively in nonrotating 3D presupernova (SN) models for over the past decade (Arnett & Meakin 2010, 2011; Müller et al. 2016; Yadav et al. 2020; Yoshida et al. 2021b). Chatzopoulos et al. (2016) considered convection in rotating burning shells in 2D for a 20 $M_\odot$ star to find that rotation can influence the total power in solenoidal modes with a larger impact of C- and O-shell regions. Recently, 3D models including rotation in the convective O-shell regions have been presented (Yoshida et al. 2021a; McNeill & Müller 2022). However, despite recent efforts, these works made approximations that present a challenge to accurately capturing the transport of AM near the end of the star's life. In the work of McNeill & Müller (2022) they excised the iron core and part of the Si shell and the simulation of Yoshida et al. (2021a) was only able to capture the final ∼92 s prior to collapse. The consequences of these approximations can affect our understanding of the AM transport within the core and potentially alter the final outcome of the star.

The AM distribution in the stellar interior is an important aspect in predicting the properties of the compact remnant (Ma & Fuller 2019). Summa et al. (2018) have also shown that the initial pre-SN AM profile, specifically the structure of the Si/Si-O interface, can lead to *qualitative* differences, i.e., (explosion versus implosion) in 3D rotationally supported core-collapse supernova (CCSN) explosion models. The differences arising from such uncertainties also have a direct impact on the mass distribution of compact objects relevant to current and next-generation gravitational wave detectors (aLIGO, VIRGO; Gossan et al. 2016; Pan et al. 2018; Belczynski et al. 2020).

In this Letter, I present a first exploratory 3D hydrodynamical simulation of the collapse of rapidly rotating 16 $M_\odot$ star to follow the evolution of the AM of the iron core and surrounding convective burning shells. I directly compare my 3D simulation to predictions made by an equivalent 1D MESA model. I show that the AM profile in convective regions can differ significantly between 1D and 3D due to the efficiency of turbulent AM transport. I find that despite the difference in the AM profile, the neutron star spin period estimate between the two models can agree to less than 5%. For different progenitors, however, such as those with tightly coupled Si/O convective shells, inferred properties of the compact remnant, specifically the natal remnant spin rate, could disagree with MESA significantly.

This paper is organized as follows: in Section 2 I discuss the computational method and initial model, in Section 3 I present the results of the 3D simulation, and in Section 4 I summarize the main results.

2. Computational Methods and Initial Models

I employ the FLASH simulation framework for my 3D stellar hydrodynamic model and utilize the Spark hydrodynamics solver (Fryxell et al. 2000; Couch et al. 2021). The Spark hydrodynamic solver uses the weighted, essentially nonoscillatory method

[4] Feynman Fellow.

(Shu 2009) fifth-order solver (WENO-5) for spatial reconstruction, a second-order strong stability preserving the Runge–Kutta time integrator, and an HLLC approximate Riemann solver.

I assume a spherically symmetric (including only the monopole term $\ell = 0$) self-gravitating potential that includes post-Newtonian corrections (Marek & Janka 2009). I use the 21 isotope approximate nuclear reaction network implemented in FLASH (Timmes & Swesty 2000; Couch et al. 2015) which includes updated tables for weak reactions (Langanke & Martínez-Pinedo 2000). My 3D simulation also uses the Helmholtz equation of state for a stellar plasma that has been used extensively (Timmes et al. 2000).

The 3D FLASH hydrodynamic simulation does not artificially enhance weak rates, covers the full 4π solid angle of the star out to a spatial extent of 100,000 km along an arbitrary Cartesian axis and utilizes the same nuclear reaction network for the entire domain—i.e., I do not excise the iron core or map it to the MESA model. I use an adaptive mesh refinement grid with 8 levels of refinement. The finest grid spacing is $\Delta x = 24$ km out to a radius of $r \approx 2400$ km (effective angular resolution of $\delta r/r \approx 1.^{\circ}6$), this radius encompasses the entire iron core and Si-burning shell.

As the FLASH input I evolve a $m_{\rm ZAMS} = 16\,M_{\odot}$ solar metallicity ($Z = 0.02$) stellar model using the Modules for Stellar Evolution Toolkit (MESA-r15140; Paxton et al. 2011, 2013, 2015, 2018). This model is initialized with an equatorial velocity of 350 km s^{-1} at the surface at a point near the zero-age main sequence. We include different mixing processes and efficiencies following the values used in Farmer et al. (2016) as well as magnetic torques via the ST dynamo (Heger et al. 2005). The stellar model is evolved from the pre-main sequence to a time approximately 725 s prior to iron core collapse as determined by MESA as the point in time at which any region of the iron core experiences an infall velocity $\geqslant$1000 km s^{-1}.

In Figure 1 I plot various stellar structure properties of the initial 1D MESA model at the time of mapping into FLASH. In the top panel, we show the convective velocity according to mixing length theory (MLT, for an $\alpha_{\rm MLT} = 1.6$ used throughout all convective regions in our 1D MESA model) and the specific nuclear energy generation rate. The convective O-shell region at mapping is shown in each panel denoted by a blue shaded region (spanning from $m \approx 1.95$–$2.76\ M_{\odot}$). I see that in this region MLT predicts a peak convective speed of $v_{\rm conv.} \approx 90$ km s^{-1} at mapping. I show the specific AM and the angular velocity in the middle panel. At the time of mapping the angular velocity shows speeds of $\omega \approx 260$ mHz in the iron core and $\omega \approx 12$ mHz in the O-shell region. The rotational and convective velocity speeds in the O-shell region are comparable at this point in time. I can compute the convective turnover timescale in this region as $t_{\rm conv.,O} \approx \Delta r_{\rm O}/v_{\rm conv.,O} \approx 159$ s. In the bottom panel of Figure 1 I show the mass-fraction profiles of our input MESA model showing the most dominant isotopes. Beneath the convective O-shell region lies a narrow Si-shell burning region. Our model shows an iron core mass of $M_{\rm Fe} \approx 1.46\ M_{\odot}$ at the time of mapping.

I follow the methods described in Zingale et al. (2002) for mapping the 1D initial model into our 3D FLASH domain. To initiate convection in the O-shell I use the methods described in O'Connor & Couch (2018) in which I choose a scaling factor and spherical harmonic degree ℓ to apply perturbations to the velocity field. I choose an ℓ of 9 and a scaling factor C such that the angle average velocity reproduces 5% of the convective velocity speed as predicted by MESA at mapping. Because of the narrow Si-shell burning region and the low convective speeds I do not apply initial perturbations to the Si-shell region. Constant angular velocity as a function of radial coordinate (shellular rotation) is assumed initially in the 3D FLASH simulation using the 1D profile as provided by MESA. In FLASH, rotation is implemented to be about the y-axis.

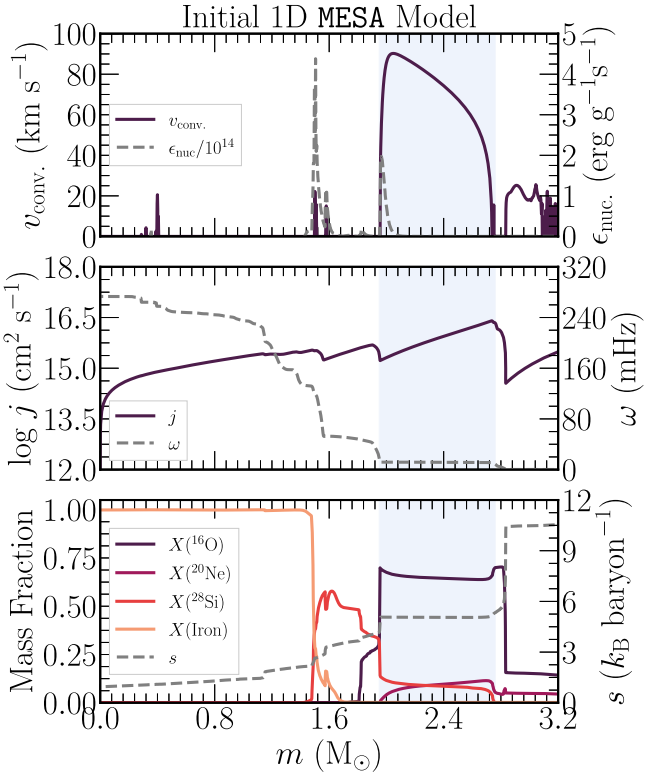

Figure 1. Stellar structure profiles for the 16 $M_{\odot}$ MESA model at the time of mapping into FLASH. Top panel: convective velocity according to MLT and specific nuclear energy generation rate as a function of mass coordinate. Middle panel: specific angular momentum and angular velocity. Bottom panel: mass-fraction profiles and the specific entropy. The convective O-shell region is shown by the shaded blue region in each panel.

3. 3D Collapse of a Rotating 16 $M_{\odot}$ Star

I follow the 3D hydrodynamic evolution up to and including gravitational instability and iron core collapse in our FLASH simulation. The simulation is evolved for a total of $t \approx 602$ s at which point the core has begun to experience iron core collapse and has reached an infall velocity of 1595 km s^{-1}. In Figure 2 I show the integrated kinetic and nuclear energy for the 3D FLASH simulation. I note an initial transient phase in the radial kinetic energy that shows a local maxima at $t \approx 100$ s. Following this time, the 3D simulation shows a quasisteady state represented by a balance between driving nuclear energy generation and the kinetic energy in the convective O-shell region. At a time beyond $t \geqslant 500$ s contraction of the iron core begins to accelerate, leading to an overall increase in the total kinetic energy and overall decrease of the net nuclear energy due to an increase in the negative specific energy generation rate in the iron core.

3.1. Characterizing the Convection and Flow Morphology

To characterize the scale of the convective eddies, I decompose the fluctuating component of the radial velocity

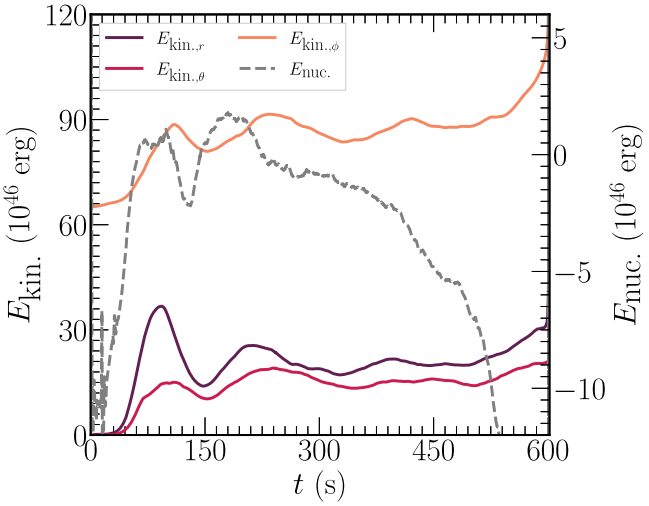

Figure 2. Time evolution of the integrated kinetic (left) and nuclear (right) energy for the duration of the 3D FLASH simulation.

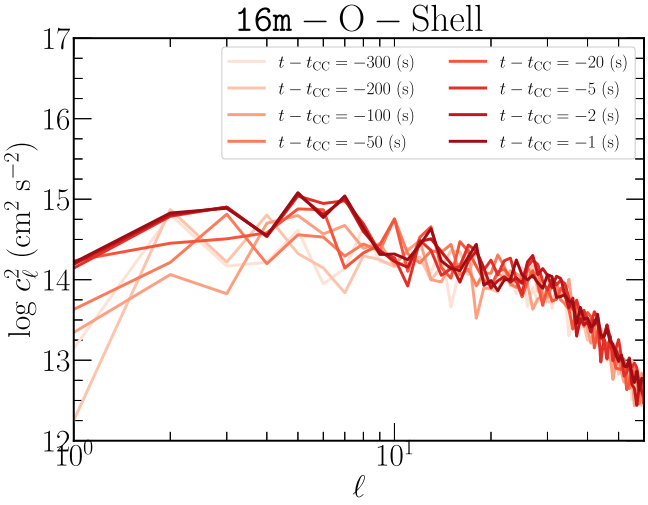

Figure 3. Time evolution of the power spectrum for the spherical harmonic decomposition of the turbulent radial velocity field for the convective O-shell region. The spectra are evaluated in the 3D model at eight different times at a radius of $r_{\rm O\text{-}shell} = 6000$ km.

field into spherical harmonics (Schaeffer 2013). The total power in a given mode is given by

$$c_\ell^2 = \sum_{-\ell}^{\ell} \left| \int Y_\ell^m(\theta, \phi) v'_{\rm rad.}(r_{\rm O-shell}, \theta, \phi) d\Omega \right|^2, \quad (1)$$

where Y_ℓ^m is a given spherical harmonic of degree ℓ and order m. The turbulent radial velocity $v'_{\rm rad.}$ is computed as $v'_{\rm rad.} = v_{\rm rad.} - \langle v_{\rm rad.} \rangle$, where the closed brackets denote an angle average of a given quantity. For the convective O-shell region I choose a value of $r_{\rm O\text{-}shell} = 6000$ km.

In Figure 3 I show the time evolution of the power of the spherical harmonic decomposition for the turbulent radial velocity field for eight different times in the 3D FLASH model. At $t - t_{\rm CC} = -300$ s, the spectra show a peak at $\ell = 2$ suggesting the bulk of the radial kinetic energy is stored at the largest scales. For the last 300 s, a steady increase in power is observed in the lowest modes ($\ell = 1$–3). As the model approaches collapse, the peak shifts to $\ell = 5$ at approximately 2 s prior to collapse. The dominant modes containing the most power are $\ell = 2$, 3, 5 and $\ell = 7$ one second before collapse. In Figure 4 I show a streamlines of the magnitude of the velocity field depicting the qualitative structure of the convective O-shell region at $t \approx 595.5$ s, $\approx$7 s prior to core collapse.

The Solberg–Høiland (SH) instability can arise in regions of significant rotational shear. This instability can work to stabilize convection in a region that would otherwise be unstable due to the Ledoux criterion (Stothers & Chin 1973; Pajkos et al. 2019). The contribution of this gradient would be considered an additional term to the Brunt-Väisälä frequency N^2 (Endal & Sofia 1978; Heger et al. 2000),

$$N_\Omega^2 = r^{-3} \frac{d}{dr}(j_y^2) \geqslant 0. \quad (2)$$

In our 3D simulation I find that the magnitude of the shear is not sufficient to significantly alter the convection in the O-shell region and that near collapse the specific AM gradient tends toward a uniform value thus moving further from a region where the SH would be relevant.

Differential rotation was found to operate in 3D simulations of O-shell burning (McNeill & Müller 2022). In their model, they observed a Rossby number of $\approx$0.24–0.4 during the quasisteady convection state. Here, I can define the convective Rossby number as

$$\mathbf{Ro} = \frac{\bar{v}_{\rm conv.}}{2\bar{\omega}\Delta r}, \quad (3)$$

where the bar denotes averages over the convective O-shell region and Δr corresponds to the width of the O-shell. In our simulation we observe a value of $Ro \approx 0.15$ at a time $t \approx 420$ s.

3.2. Angular Momentum Transport

To begin, I compute the integrated y-component of AM contained in our 3D domain at $t = 0$ and compare this to the point at collapse to assess the AM conservation throughout our simulation. In doing so, I find an initial value of $J_y(t=0) \approx 2.76 \times 10^{49}$ g cm^2 s^{-1}. At a time of $t \approx 200$ s, I compute a total of $J_y(t = 200) \approx 2.74 \times 10^{49}$ g cm^2 s^{-1} and at the end of the simulation, $J_y(t = t_{\rm CC}) \approx 2.70 \times 10^{49}$ g cm^2 s^{-1}. This result suggests a loss of 2.4% of the total y-component of AM over the duration of the simulation. McNeill & Müller (2022) estimate AM conservation of $\approx$11% for their rotating 3D O-shell simulation.

In Figure 5 I show the time evolution of the angle-averaged y-component of the specific AM (j_y) from our 3D simulations at five different times during the simulation. The approximate extent of the convective Si- and O-shell region is denoted by the blue shading. Because the 3D simulation collapses $\approx$123 *earlier* than predicted by MESA, I compare our 3D profiles at collapse to a MESA 1D profile that most closely matches the central density at the point of comparison. The MESA models used for comparison was also started from the point of mapping into FLASH and evolved to CC *without* the ST dynamo as magnetic fields are not considered in the 3D simulation presented here.

In general, I find that AM profile in the iron core (inner $m \lesssim 1.6 M_\odot$) remains constant in shape only, showing a slight decrease in the core from $t = 0$ to the point of collapse. The MESA model shows a decrease in AM over this time as AM appears to be diffused out to the outer Si-shell region. At a mass coordinate range corresponding to the Si-shell region, $m \approx 1.6$–$1.95 M_\odot$ I notice two things in the 3D angle average

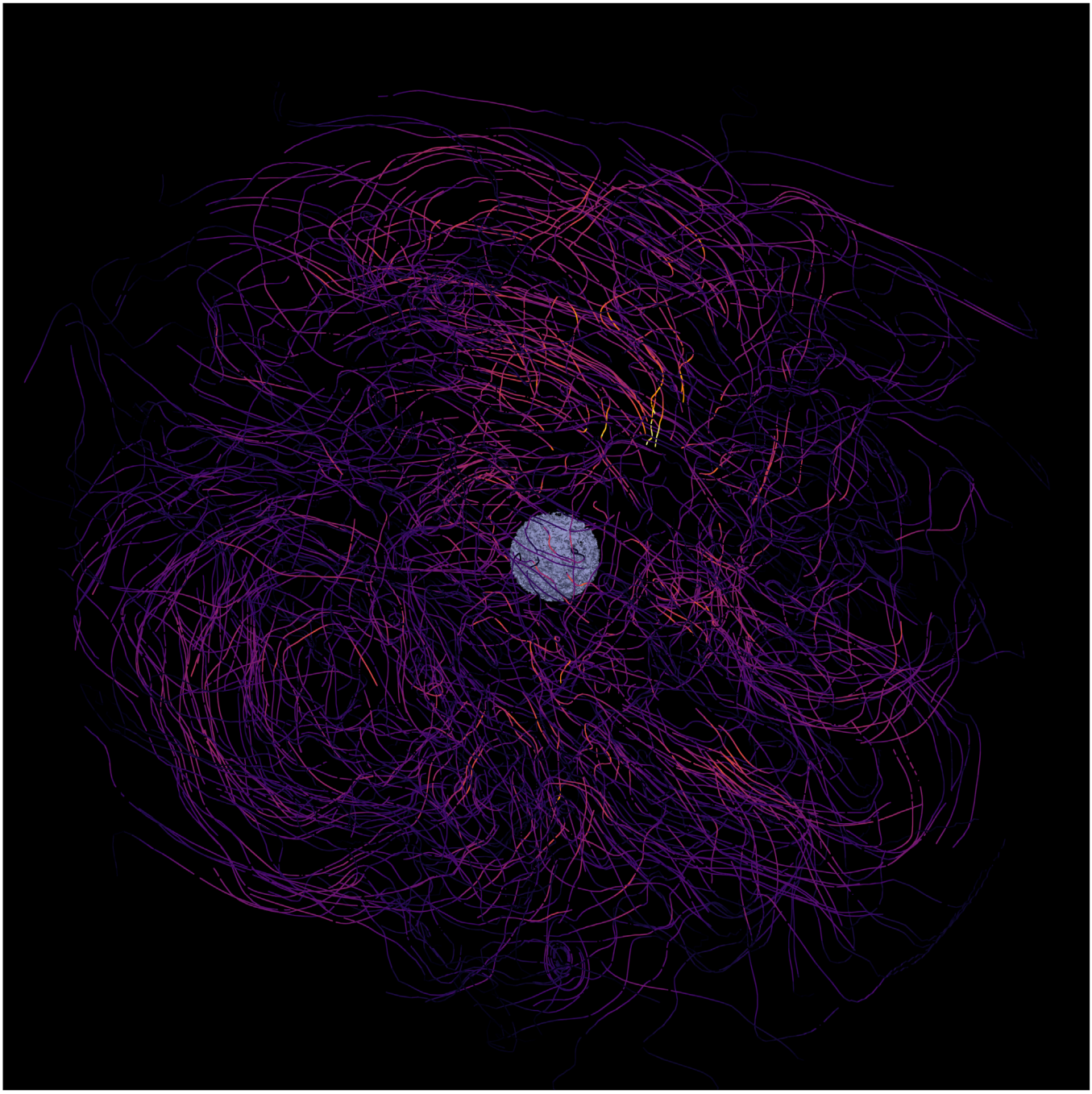

Figure 4. Streamlines of the magnitude of the velocity field for the 3D FLASH simulation at a time ≈7 s before iron core collapse. The purple contour shows the iron core at a radius of $r \approx 2400$ km shown here. The brighter (orange) stream lines correspond to speeds of $|\boldsymbol{v}| \approx 800$ km s^{-1}. The orientation of the rendering is shown with the north vector aligned with the y-axis, the axis of rotation, (with a slight horizontal offset). Large-scale flow is observed with streamlines wrapping about the axis of rotation out to the edge of the convective shell region. The spatial scale of the image corresponds to a spatial extent of ≈40,000 km on a side. This image was produced using Paraview.

AM profiles. First, the steep gradient at $t = 0$ is smoothed out and tends toward a uniform profile near the active and at some points convective Si-shell burning region ($m \approx 1.6$–$1.7 M_\odot$). Second, beyond this mass coordinate ($m \approx 1.7$–$1.95 M_\odot$), the 3D model is not convective and the AM profile does not vary significantly over time. The AM profile matches closely for the 3D profile at $t = 0$ to that of the 1D MESA profile but shows less AM in this region at collapse.

I observe a similar feature in the convective O-shell region, $m \approx 1.95$–$2.76 M_\odot$ where the steep AM gradient is smoothed efficiently (as quickly at $t = 200$ s) and the *sign* of the AM gradient at the base of the O-shell is reversed and maintained until collapse. Throughout most of the convective O-shell region the profile tends toward a uniform profile near $\log \langle j_y \rangle \approx 16$ g cm^2 s^{-1}. Beyond the convective O shell, the profile shape matches well to the initial configuration given by MESA as no active convection is occurring in the 3D simulation or 1D MESA model.

One can determine the relevant contribution of AM transport in the convective O-shell region by considering the Favre-average AM transport equations. Here, I follow the methods described in McNeill & Müller (2022) and whose derivation is

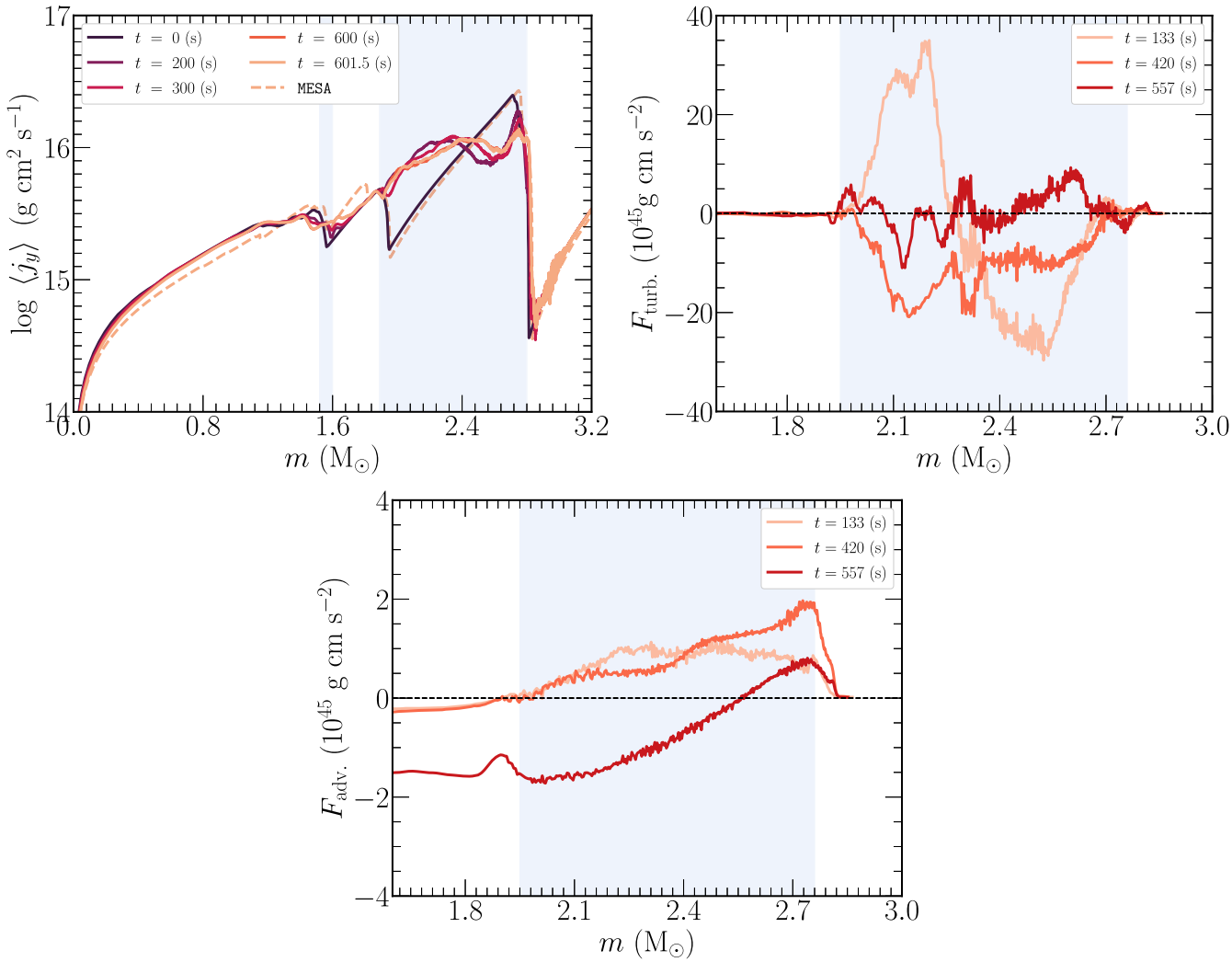

Figure 5. Top left: angle average of the y-component of the specific angular momentum for the 3D FLASH simulation at five different times include $t = 601.5$ s (half a second before iron core collapse). The correponding MESA model is also shown by the dashed gray line chosen to match the central density of the 3D model at $t = 601.5$ s. Turbulent ($4\pi r^2 F_{\rm turb.}$, top right) and advective flux ($4\pi r^2 F_{\rm adv.}$, bottom left) terms for the 3D simulation at three different times. The approximate convective Si- ($m \approx 1.52$–$1.60\ M_\odot$) and O-shell ($m \approx 1.89$–$2.80\ M_\odot$) regions at $t = 601.5$ are denoted by the blue shading.

described in detail in McNeill & Müller (2020). In this study I only present the two relevant terms for AM transport in the O shell,

$$\frac{\partial \langle \rho \boldsymbol{j}_y \rangle}{\partial t} + \nabla \cdot \boldsymbol{F}_{\rm adv.} + \nabla \cdot \boldsymbol{F}_{\rm turb.} = 0. \quad (4)$$

The advective flux can be computed as

$$F_{\rm adv.} = \rho \tilde{v}_{\rm r} \tilde{j}_y, \quad (5)$$

where $v_{\rm rad.}$ is again the radial velocity and j_y is the $y-$component of the specific AM magnitude. Here, the tilde defines a Favre-averaged quantity (Favre 1965) $\tilde{X}$ as

$$\tilde{X} = \frac{\int \rho X {\rm d}\Omega}{\int \rho {\rm d}\Omega}. \quad (6)$$

The turbulent flux component can be computed as,

$$F_{\rm turb.} = \langle \rho v_{\rm r}'' j'' \rangle. \quad (7)$$

I adopt the same notation given in McNeill & Müller (2020) where $X'' = X - \tilde{X}$.

In Figure 5 I plot the resulting advective (*bottom*) and turbulent (*top right*) fluxes at $t = 113$ s (once convection has been established), $t = 420$ s (toward the end of the quasisteady convective state in the O shell) and $t = 557$ s (as the model approaches collapse and evolves out of dynamical equilibrium). At the earliest time considered I observe a positive flux (positive $v_{\rm rad.}''$) in the O shell at $m \approx 1.9$–$2.3\ M_\odot$ that peaks at $\approx 3 \times 10^{46}$ g cm s^{-2}, from $m \approx 2.3$–$2.8\ M_\odot$ the same magnitude is found but for a negative flux. At this point in time, the turbulent component is causing the observed change in the AM profile throughout the convective O shell observed in Figure 5.

For $t = 420$ s, I observe a negative flux across the entire convective O-shell region with a peak value of $\approx 2 \times 10^{46}$ g cm s^{-2}. At this time, the AM profile appears to have reached a new equilibrium in the redistribution with a modest net flux inward. For the final time considered, the magnitude of the flux decreases to about $\approx 1 \times 10^{46}$ g cm s^{-2} suggesting turbulent transport has become less efficient except for at a mass coordinate of $m \approx 2.4$–$2.7\ M_\odot$ where a significant AM gradient still exists but turbulent radial velocity speeds are lower and require a longer time to homogenize the AM profile.

The advective flux component (bottom panel of Figure 5) shows positive flux for times $t = 133$ s and $t = 420$ s across the entire O-shell region with a peak value near the edge of the O-shell of $4\pi r^2 F_{\rm adv.} \approx 2 \times 10^{45}$ g cm s^{-2}. These values suggest advection of AM out of the convective O-shell region also observed via the gradual decrease over time of the peak of the specific AM at the outer convective boundary in Figure 5. At $t = 557$ s, a negative flux is found with magnitude of $\approx 2 \times 10^{45}$ g cm s^{-2} over most of the O-shell. The shift toward a negative flux for this term is likely attributed to the acceleration of the contraction leading to an increase of the inward (negative) radial velocity in the O shell.

At late times ($t \lesssim 300$ s before collapse), the Si shell is convective over a thin region. Within this region, a positive turbulent flux is observed which helps homogenize the AM profile in a similar fashion to that of the O shell. However, the turbulent flux component in this region is found to be an order of magnitude less than those in the O shell due to lower turbulent radial velocity speeds and leads to a longer time needed for the AM profile to readjust. For example, in Figure 5 at $t = 200$ s the AM profile in O-shell region is qualitatively different and the gradient at the convective boundary has changed sign. However, the nonconvective Si-shell region ($m \approx 1.6$–$1.95 M_\odot$) still shows partial correspondence to the shape of the MESA AM profile up to the point of collapse. Near the convective Si-shell burning region ($m \approx 1.5$–$1.6 M_\odot$), the AM profile begins to deviate from the 1D MESA profile moving closer toward uniform in the evolution toward collapse.

3D models of rotationally supported CCSN explosions were shown to lead to qualitative differences when considering different AM profiles (Summa et al. 2018). In their comprehensive study, Summa et al. (2018) found that only their "artifical rotation" model which utilized an enhanced AM profile was able to reach the conditions for shock revival and explosion as compared to an AM profile from a 1D stellar evolution model. The determining factor was the time at which the Si/Si-O interface was accreted onto the shock. The results of their study suggest a crucial dependence on the specific AM profile in the Si-/O-shell convective regions near collapse. The efficient transport of AM facilitated by convection in the 3D model considered here is a first step in understanding the impact such progenitor models might have on models of CCSNe.

3.3. Proto-neutron Star Mass and Spin Estimates

The AM profile predicted from stellar evolution models can be used to determine properties of the proto-neutron star (PNS) or black hole (BH) borne as a result of stellar core collapse. Following Heger et al. (2005), I compute inferred PNS properties using the 3D rotating model presented here as well as the 1D equivalent MESA model. I assume a 12 km neutron star and a moment of inertia of the form $I \approx 0.35 M_{\rm grav} R^2$ for the estimates presented here. For both models I find $M_{\rm grav.} \approx 1.58\ M_\odot$ and $M_{\rm bary.} \approx 1.88\ M_\odot$ for the gravitational and baryonic mass values, respectively. The resulting period for the 3D model at $t = 602$ s is found to be 1.57 ms, agreeing with the estimate for the MESA model to within ≈1%. When using a fixed mass cut of $M_{\rm grav.} \approx 1.4\ M_\odot$ and $M_{\rm bary.} \approx 1.7\ M_\odot$ for both models, a larger difference is observed with MESA predicting a ≈5% longer period.

While I find agreement with MESA in the natal PNS spin rate for the 3D progenitor model considered here, models with different Si/O convective structures might lead to larger differences in the integrated AM profile. Such profiles are crucial in predicting natal BH and PNS spin rates and also sensitive to input physics in 1D stellar models. The combination of these uncertainties present a challenge in our predictive capability in describing the mass distribution and spin rates of binary NS and binary BH systems observed by Advanced LIGO (Belczynski et al. 2020). Rotating 3D CCSN progenitor models such as the exploratory model presented here represent a necessary step toward addressing these challenges.

4. Summary and Discussion

I have presented the evolution of the AM distribution in the final 10 minutes before iron core collapse in a rapidly rotating $16\,M_\odot$ star revealed by a 4π 3D hydrodynamic simulation. For the first time, we were able to directly compare AM profile in the stellar core and surrounding convective shells in our 3D simulation to a 1D model predicted by MESA. It was shown that despite the different dynamical evolution of the stellar core in the 3D simulation, the PNS spin-period estimate at core collapse can agree with MESA less than 5%. For different progenitor models, however, such as those with tightly coupled Si/O convective shells, the efficient AM distribution in 3D simulations may lead to differences in the inferred remnant properties as compared to MESA.

Angular momentum transport was found to be facilitated in the convective O-shell region via a positive turbulent flux allowing the shape of the profile to reach a nearly uniform specific angular momentum within a single convective turnover time. In nonconvective Si-rich regions it was shown that the profile matched well to MESA. Near the convective Si-shell region of the 3D model, the AM profile began to diverge from the shape predicted by MESA but on a slower timescale due to the lower turbulent speeds when compared to the O-shell region.

At collapse, the peak of the turbulent velocity spectrum is found at spherical harmonic degree $\ell = 5$. Recent work by Yoshida et al. (2021a) observed large-scale spiral arms emerge prior to collapse in the rotational kinetic energy density distribution. We did not identify such spiral arm structures in the 3D model presented here. As with the presence of large-scale modes in the convective shells near collapse, rotation is a crucial component and must be taken into consideration in ordinary 3D CCSN progenitor models and those that might produce more luminous transients.

The consequences of the AM transport observed in the 3D model presented here could *qualitatively* alter rotationally supported CCSN explosion dynamics and inferred remnant properties. The exploratory 3D model presented here is a first step in considering the effects of rotation within the stellar core and surrounding convective shells. Long-term, high-resolution models informed by a range of initial 1D models will be necessary to determine the complex interplay of turbulence, rotation, and convection in the fate of a massive star.

The author thanks Sean Couch, Josh Dolence, and Philipp Edelmann for useful discussions. Research presented in this article was supported by the Laboratory Directed Research and Development program of Los Alamos National Laboratory under project number 20210808PRD1. This work was supported in part by Michigan State University through computational resources provided by the Institute for Cyber-

Enabled Research. This research made extensive use of the SAO/NASA Astrophysics Data System (ADS).

Software: `MESA` (Paxton et al. 2011, 2013, 2015, 2018, http://mesa.sourceforge.net), `FLASH` (Fryxell et al. 2000, http://flash.uchicago.edu/site/), `yt` (Turk et al. 2011, https://yt-project.org), and `matplotlib` (Hunter 2007, https://matplotlib.org).

ORCID iDs

C. E. Fields https://orcid.org/0000-0002-8925-057X

References

Arnett, W. D., & Meakin, C. 2010, in IAU Symp. 265, Chemical Abundances in the Universe: Connecting First Stars to Planets (Dordrecht: Reidel), 106
Arnett, W. D., & Meakin, C. 2011, ApJ, 733, 78
Belczynski, K., Klencki, J., Fields, C. E., et al. 2020, A&A, 636, A104
Chatzopoulos, E., Couch, S. M., Arnett, W. D., & Timmes, F. X. 2016, ApJ, 822, 61
Couch, S. M., Carlson, J., Pajkos, M., et al. 2021, ParC, 108, 102830
Couch, S. M., Chatzopoulos, E., Arnett, W. D., & Timmes, F. X. 2015, ApJL, 808, L21
Davis, A., Jones, S., & Herwig, F. 2019, MNRAS, 484, 3921
de Mink, S. E., Langer, N., Izzard, R. G., Sana, H., & de Koter, A. 2013, ApJ, 764, 166
Endal, A. S., & Sofia, S. 1978, ApJ, 220, 279
Farmer, R., Fields, C. E., Petermann, I., et al. 2016, ApJS, 227, 22
Favre, A. J. 1965, JAM, 32, 241
Fryxell, B., Olson, K., Ricker, P., et al. 2000, ApJS, 131, 273
Fukuda, I. 1982, PASP, 94, 271
Gossan, S. E., Sutton, P., Stuver, A., et al. 2016, PhRvD, 93, 042002
Heger, A., Langer, N., & Woosley, S. E. 2000, ApJ, 528, 368
Heger, A., Woosley, S. E., & Spruit, H. C. 2005, ApJ, 626, 350
Hunter, J. D. 2007, CSE, 9, 90
Jones, S., Andrassy, R., Sandalski, S., et al. 2017, MNRAS, 465, 2991
Langanke, K., & Martínez-Pinedo, G. 2000, NuPhA, 673, 481
Ma, L., & Fuller, J. 2019, MNRAS, 488, 4338
Marek, A., & Janka, H.-T. 2009, ApJ, 694, 664
McNeill, L. O., & Müller, B. 2020, MNRAS, 497, 4644
McNeill, L. O., & Müller, B. 2022, MNRAS, 509, 818
Müller, B., Viallet, M., Heger, A., & Janka, H.-T. 2016, ApJ, 833, 124
O'Connor, E. P., & Couch, S. M. 2018, ApJ, 854, 63
Pajkos, M. A., Couch, S. M., Pan, K.-C., & O'Connor, E. P. 2019, ApJ, 878, 13
Pan, K.-C., Liebendörfer, M., Couch, S. M., & Thielemann, F.-K. 2018, ApJ, 857, 13
Paxton, B., Bildsten, L., Dotter, A., et al. 2011, ApJS, 192, 3
Paxton, B., Cantiello, M., Arras, P., et al. 2013, ApJS, 208, 4
Paxton, B., Marchant, P., Schwab, J., et al. 2015, ApJS, 220, 15
Paxton, B., Schwab, J., Bauer, E. B., et al. 2018, ApJS, 234, 34
Ramírez-Agudelo, O. H., Simón-Díaz, S., Sana, H., et al. 2013, A&A, 560, A29
Schaeffer, N. 2013, GGG, 14, 751
Shu, C.-W. 2009, SIAMR, 51, 82
Spruit, H. C. 2002, A&A, 381, 923
Stothers, R., & Chin, C.-W. 1973, ApJ, 179, 555
Summa, A., Janka, H.-T., Melson, T., & Marek, A. 2018, ApJ, 852, 28
Timmes, F. X., Hoffman, R. D., & Woosley, S. E. 2000, ApJS, 129, 377
Timmes, F. X., & Swesty, F. D. 2000, ApJS, 126, 501
Turk, M. J., Smith, B. D., Oishi, J. S., et al. 2011, ApJS, 192, 9
Yadav, N., Müller, B., Janka, H. T., Melson, T., & Heger, A. 2020, ApJ, 890, 94
Yoshida, T., Takiwaki, T., Aguilera-Dena, D. R., et al. 2021a, MNRAS, 506, L20
Yoshida, T., Takiwaki, T., Kotake, K., et al. 2021b, ApJ, 908, 44
Zingale, M., Dursi, L. J., ZuHone, J., et al. 2002, ApJS, 143, 539